A Whole-Brain Map and Assay Parameter Analysis of Mouse VTA Dopaminergic Activation

Horea-Ioan Ioanas[1] Bechara John Saab[2] Markus Rudin[1]
[1]Institute for Biomedical Engineering, ETH and University of Zurich
[2]Preclinical Laboratory for Translational Research into Affective Disorders, DPPP, Psychiatric Hospital, University of Zurich

Abstract — Ascending dopaminergic projections from neurons located in the Ventral Tegmental Area (VTA) are key to the etiology, dysfunction, and control of motivation, learning, and addiction. Due to evolutionary conservation of this nucleus and the extensive use of mice as disease models, establishing an assay for VTA dopaminergic signalling in the mouse brain is crucial for the translational investigation of neuronal function phenotypes of diseases and interventions. In this article we use optogenetic stimulation for VTA dopaminergic neuron stimulation, in combination with functional Magnetic Resonance Imaging (fMRI), a method widely used in human deep brain imaging. We present the first whole-brain opto-fMRI map of dopaminergic activation in the mouse, and show that VTA dopaminergic system function is consistent with but diverges in a few key aspects from its structure. While the activation map predominantly includes and excludes target areas according to their relative projection densities (e.g. strong activation of the nucleus accumbens and low activation of the hippocampus), it also includes areas for which a structural connection is not well established (such as the dorsomedial striatum). We further detail assay variability with regard to multiple experimental parameters, including stimulation protocol and implant position, and provide detailed evidence-based recommendations for assay reuse.

Background

The dopaminergic system consists of a strongly localized, and widely projecting set of neurons (fig. 1a). On account of the small number of dopaminergic neurons ($\approx 300,000$ in humans [1], $\approx 10,000$ in rats [2], and $\approx 4,000$ in mice [3]), tractography commonly fails to resolve the degree centrality of this neurotransmitter system, and thus it is not commonly depicted as a significant node in graph representations of the brain. However, it is precisely the small number of widely branching and closely similar neurons, which makes the dopaminergic system a credible candidate for truly node-like function in coordinating brain activity. As is expected given such salient features, the system is widely implicated in neuropsychiatric phenomena (including addiction [4, 5], attentional control [6], motivation [7], creativity [8], personality [9], neurodegeneration [10], and schizophrenia [11]), and is a common target for pharmacological interventions. Manipulation of the dopaminergic system extends widely beyond the medical field, and includes performance-enhancement [12, 13], as well recreation [4]. As such, better and more predictively powerful models of the dopaminergic system can improve numerous aspects of human activity, in the clinic and beyond.

Experimentation in human subjects is methodologically constrained, and thus neuroscience relies on other context, such as model animal research, for cell biological insights, which are instrumental to the refinement of interventions. Due to high evolutionary conservation [20], the dopaminergic system is an excellent candidate for translational study. Of the common model animals, the mouse offers significant advantages including short generation spans, broad availability of transgenic lines, highly accessible histology, and the smallest size among mammalian model organisms. Far from trivial, this latter quality offers a significant advantage for numerous imaging techniques, including optics, optoacoustics, and magnetic resonance imaging (MRI). Furthermore, the small size greatly increases experiment scalability and multi-center reproducibility, beyond even what can be achieved using the rat model. Of particular relevance to pharmacological research, the mouse possesses a high metabolic rate, allowing for rapid drug clearance and thus high contrast in repeated drug administration sessions.

As it coordinates phenomena such as perception, decision, and action, the function of the brain is highly holistic, and this underscores the importance of whole-brain measurement techniques for its characterization. This is particularly true for monoaminergic neurotransmitter systems, where focal interventions can have wide-ranging effects. Owing to its deep penetration, high rostrocaudal coverage, and large-scale usage in human studies, fMRI is one of the foremost methods for studying dopaminergic modulation of brain function.

Imaging a neurotransmitter system comprised of a small number of cells, based only on spontaneous activity, is highly unreliable due to a very low signal to noise ratio (SNR). This limitation can, however, be overcome by introducing exogenous stimuli. While the colocalization of widely projecting dopaminergic cell bodies into nuclei makes targeting comparatively easy, dopaminergic nuclei also contain notable populations

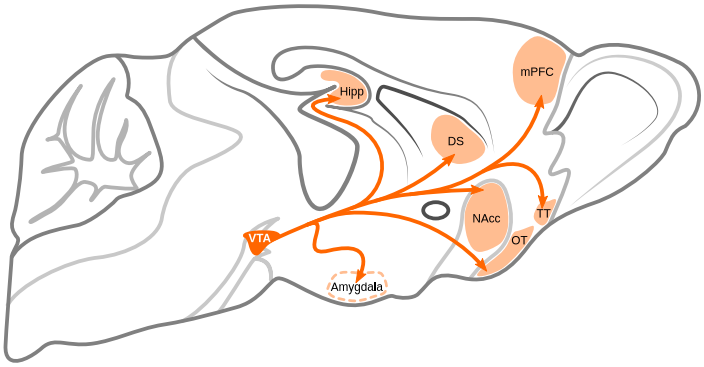

(a) Schematic map of VTA dopaminergic projections [14, 15, 16, 17, 18]. Dotted structures are off-slice, and projection arrows do not reflect actual fiber bundle paths. Abbreviations: Hipp (Hippocampus), DS (Dorsal Striatum), NAcc (Nucleus Accumbens), OT (Olfactory Tuberculum), mPFC (medial Prefrontal Cortex), TT (Tenia Tecta).

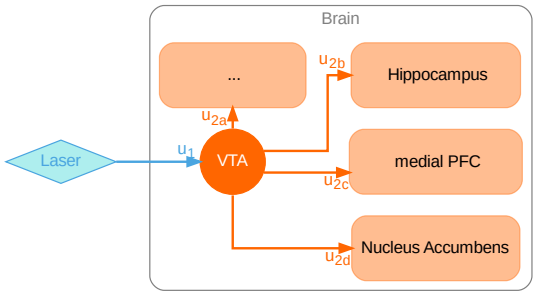

(b) Simplified network model of 1-step signal relay following optogenetic stimulation of the VTA. The u_1 weighting corresponds to VTA somatic excitability and u_{2a}, u_{2b}, u_{2c} and u_{2d} correspond to transmission at the dopaminergic synapses in the respective projection areas.

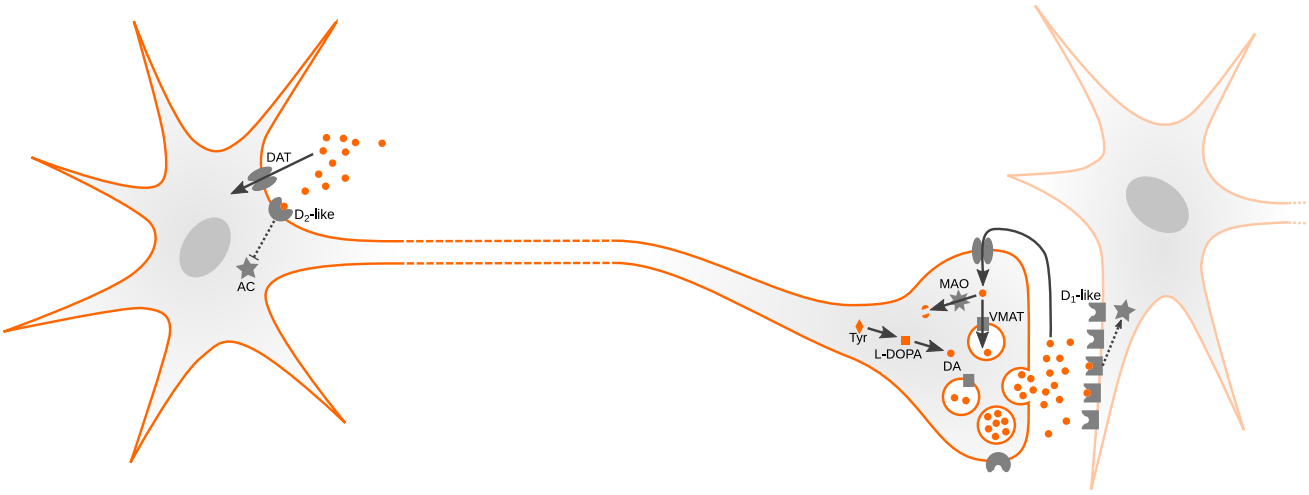

(c) Schematic overview of VTA dopaminergic neurons, with the soma located in the VTA and synapses in one or multiple other projection area voxels. Excitability at the soma are contingent on D_2 autoinhibition, while transmission at the synapse is contingent on dopamine metabolism, turnover, and postsynaptic D_1 expression. Abbreviations: AC (adenylyl cyclase), DA (dopamine), DAT (dopamine transporter), MAO (monoamine oxydase), VMAT (vesicular monoamine transporter), Tyr (tyrosine) [19].

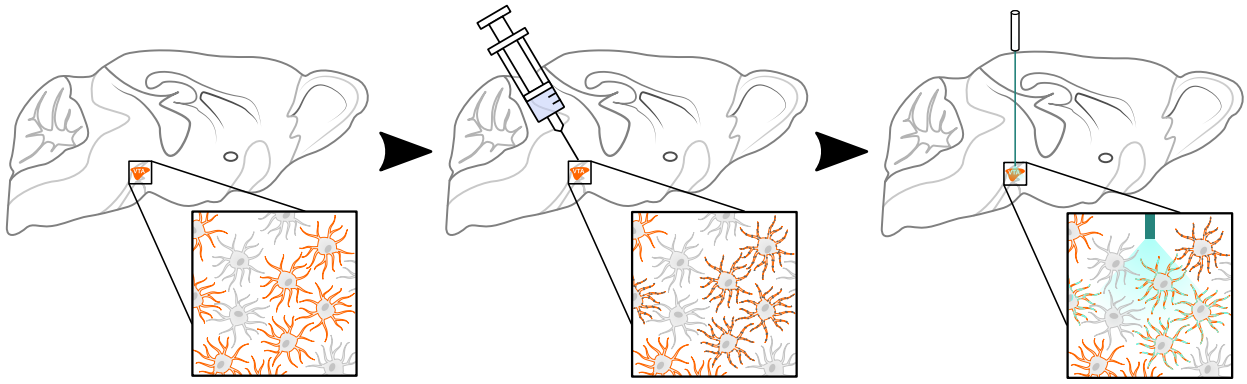

(d) Schematic of optogenetic cell selection and activation. Orange denotes dopaminergic cells, gray enlarged elements on the cell periphery indicate channelrhodopsin expression, and cyan segments on the cell periphery denote depolarization events.

Figure 1: The cell biological compartmentalization of dopaminergic neurotransmission (and susceptibility to psychopharmacology) can partly be mapped onto neuroanatomical features by a simple network model, using optogenetics. Depicted are schematic overviews of the VTA dopaminergic system at various spatial resolutions.

of non-dopaminergic cells. Activating such cells may confound an intended dopaminergic read-out, as they exhibit different kinetics, especially with regard to psychopharmacology [21]. In order to specifically target dopaminergic cells, they need to be sensitized to an otherwise inert stimulus in a transcription-dependent manner. This can be achieved via optogenetics, a method based on light-stimulation of cells expressing light-sensitive proteins such as channelrhodopsin [22]. Cell-type selectivity can be achieved by Cre-conditional channelrhodopsin vector delivery [23] to transgenic animals expressing Cre-recombinase under a dopaminer-

gic promoter. Following protein expression, stimulation can be delivered via an implanted optic fiber. The combination of this stimulation method with fMRI is commonly referred to as opto-fMRI [24, 25].

The majority of dopaminergic cell bodies are clustered in the midbrain into two lateralized nucleus pairs, the Ventral Tegmental Area (VTA) and Substantia Nigra pars compacta (SNc). Of these, the VTA displays a wider distribution of efferents (fig. 1a), whereas the SNc projects primarily to the dorsal striatum [18].

The most popular means of producing spatially resolved sensitivity summaries from fMRI, and opto-fMRI in particular, is general linear modelling (GLM) of stimulus evoked activity [26]. For this purpose, a precisely specified stimulus train is presented to the brain, and convolved with an impulse response function (IRF, also called hemodynamic response function) for analysis. Subsequently, a mass univariate regression analysis is performed across all voxels, allowing them to be assigned parameter values, which denote the strength of activation adjusted for the sample noise. While powerful, this approach implies that all voxels in the brain are exposed in an indistinguishable fashion to the stimulation, a questionable assumption in view of the actual network architecture. Particularly in cases where stimulation is introduced via well-known pathways, a simple network model for signal transmission could be explored via seed-based functional connectivity (fig. 1b). Moreover, for neurotransmitter systems with colocalized cell bodies and long efferent projections, the macroscopic resolution of fMRI allows mapping somatodendritic processes (e.g. excitability upon depolarization at the soma) to "cell-body" voxels, and signal transmission at the synapse to "projection" voxels (fig. 1c).

This study pertaining to whole-brain modelling of VTA dopaminergic function in mice aims to produce three novel research outputs. Firstly, proof-of-principle documenting the feasibility of dopaminergic VTA opto-fMRI in the mouse should be demonstrated, and results should be compared and contrasted to present knowledge regarding structural projections. Secondly, controlled methodological variation effects should be described and evaluated, to lay a reliable and well-informed foundation for the technique, allowing its reuse as a general-purpose dopaminergic system assay. Lastly, a reference neurophenotype of stimulus-evoked dopaminergic function (represented as a brain-wide voxelwise map) should be published in standard space to facilitate co-registered data integration, operative targeting, and comparative evaluation of pathology or treatment induced effects.

Methods

Animal Preparation

VTA dopaminergic neurons were specifically targeted via optogenetic stimulation. As shown in fig. 1d, this entails a triple selection process. Firstly, cells are selected based on gene expression (via a transgenic mouse strain), secondly the location is selected based on the injection site, and thirdly, activation is based on the overlap of the aforementioned selection steps with the irradiation volume covered by the optic fiber.

A mouse strain was chosen, which expresses Cre recombinase under the dopamine transporter (DAT) promoter [27]. Transgenic construct presence was assessed via polymerase chain reaction (PCR) for the Cre construct, using the forward primer ACCAGCCAGCTATCAACTCG and the reverse primer TTGCCCCTGTTTCACTATCC. A total of 24 transgenic animals and 7 control wild type animals are included in the study. The animal sample consisted of 18 males and 15 females, with a group average age of 302 days (standard deviation 143 days) at the study onset.

The right VTA (fig. 3e, green contour) of the animals was injected with a recombinant Adeno-Associated Virus (rAAV) solution. The vector delivered a plasmid containing a floxed channelrhodopsin and YFP construct: pAAV-EF1a-double floxed-hChR2(H134R)-EYFP-WPRE-HGHpA, gifted to a public repository by Karl Deisseroth (Addgene plasmid #20298). Viral vectors and plasmids were produced by the Viral Vector Facility (VVF) of the Neuroscience Center Zurich (Zentrum für Neurowissenschaften Zürich, ZNZ). The solution was prepared at a titer of 5.7×10^{12} vg/ml and volumes from 0.4 to 1.6 µl were injected into the right VTA. Injection coordinates ranged in the posteroanterior (PA) direction from −3.5 to −3.05 mm (relative to bregma), in depth from 4.0 to 4.4 mm (relative to the skull), and were located 0.5 mm right of the midline. Construct expression was ascertained post mortem by fluorescent microscopy of formaldehyde fixed 200 µm brain slices.

For optical stimulation, animals were fitted with an optic fiber implant (l = 4.7 mm d = 400 µm NA = 0.22) targeting the right VTA, at least two weeks before imaging. Implant target coordinates ranged in the PA direction from −3.5 to −3.05 mm (relative to bregma), in depth from 4.0 to 4.6 mm (relative to the skull), and were located 0.5 to 0.55 mm right of the midline.

For stimulation, an Omicron LuxX 488-60 laser (488 nm) was used, tuned to a power of 30 mW at contact with the fiber implant, according to the protocols listed in tables S1 to S7. Stimulation protocols were delivered to the laser and recorded to disk via the COSplayer device [28]. Animal physiology, preparation, and measurement metadata were tracked with the LabbookDB database framework [29].

MR Acquisition

Over the course of preparation and measurement, animals were provided a constant flow of air with an additional 20 % O_2 gas (yielding a total O_2 concentration of ≈36 %). For animal preparation, anesthesia was induced with 3 % isoflurane, and maintained at 2 to 3 % during preparation — contingent on animal reflexes. Animals were fixed to a heated MRI-compatible cradle via ear bars and a face mask equipped with a bite hook. A subcutaneous (s.c.; right dorsal) and intravenous (i.v.; tail vein) infusion line were applied. After

animal fixation, a bolus of medetomidine hydrochloride (Domitor, Pfizer Pharmaceuticals, UK) was delivered s.c. to a total dose of 100 ng/(g BW) and the inhalation anesthetic was reduced to 1.5 % isoflurane. After a 5 min interval, the inhalation anesthetic was set to 0.5 % and medetomidine was continuously delivered at 200 ng/(g BW h) for the duration of the experiment. This anesthetic protocol is closely based on extensive research into animal preparation for fMRI [30].

All data were acquired with a Bruker Biospec system (7 T, 16 cm bore), and an in-house built transmit/receive surface coil, engineered to permit optic fiber implant protrusion.

Anatomical scans were acquired via a TurboRARE sequence, with a RARE factor of 8, an echo time (TE) of 30 ms, an inter-echo spacing of 10 ms, and a repetition time (TR) of 2.95 s. Thirty adjacent (no slice gap) coronal slices were recorded with an nominal in-plane resolution of $\Delta x(\nu) = \Delta y(\phi) = 75\,\mu m$, and a slice thickness of $\Delta z(t) = 450\,\mu m$.

Functional scans were acquired with a gradient-echo EPI sequence, a flip angle of 60°, and TR/TE = 1000 ms/5.9 ms. Thirty adjacent (no slice gap) coronal slices were recorded with an nominal in-plane resolution of $\Delta x(\nu) = \Delta y(\phi) = 225\,\mu m$, and a slice thickness of $\Delta z(t) = 450\,\mu m$. Changes in cerebral blood volume (CBV) are measured as a proxy of neuronal activity following the administration of an intravascular iron oxide nanoparticle based contrast agent (Endorem, Laboratoire Guebet SA, France). The contrast agent (30.24 µg/(g BW)) is delivered as an i.v. bolus 10 min prior to the fMRI data acquisition, to achieve a pseudo steady-state blood concentration. This contrast is chosen to enable short echo-time imaging thereby minimizing artefacts caused by gradients in magnetic susceptibility.

Preprocessing

Data conversion from the proprietary ParaVision format was performed via the Bruker-to-BIDS repositing pipeline [31] of the SAMRI package (version `0.4` [32]). Following conversion, data was dummy-scan corrected, registered, and subject to controlled smoothing via the SAMRI registration workflow [33]. As part of this processing, the first 10 volumes were discarded (automatically accounting for volumes excluded by the scanner software). Registration was performed using the standard SAMRI mouse-brain-optimized parameter set for ANTs [34] (version `2.3.1`). Data was transformed to a stereotactically oriented standard space (the DSURQEC template space, as distributed in the Mouse Brain Atlases Package [35], version `0.5.3`), which is based on a high-resolution T_2-weighted atlas [36]. Controlled spatial smoothing was applied in the coronal plane up to 250 µm via the AFNI package [37] (version `19.1.05`).

The registered time course data was frequency filtered depending on the analysis workflow. For stimulus-evoked activity, the data was low-pass filtered at a period threshold of 225 s, and for seed-based functional connectivity, the data was band-pass filtered within a period range of 2 to 225 s.

Statistics and Data

Volumetric data was modelled using functions from the FSL software package [38] (version `5.0.11`). First-level regression was applied to the temporally resolved volumetric data via FSL's `glm` function, whereas the second-level analysis was applied to the first-level contrast and variance estimates via FSL's `flameo`.

Stimulus-evoked first-level regression was performed using a convolution of the stimulus sequence with an opto-fMRI impulse response function, estimated by a beta fit of previously reported mouse opto-fMRI responses [25]. Seed-based functional connectivity analysis was performed by regressing the time course of the voxel most sensitive to the stimulus-evoked activity (per scan) in the VTA region of interest.

Brain parcellation for region-based evaluation was performed using a non-overlapping multi-center labelling [36, 39, 40, 41], as distributed in version `0.5.3` of the Mouse Brain Atlases data package [35]. The mapping operations were performed by a SAMRI function, using the nibabel [42] and nilearn [43] libraries (versions `2.3.1` and `0.5.0`, respectively). Classification of implant coordinates into "best" and "rejected" categories was performed via 1D k-means clustering, implemented in the scikit-learn library [44] (version `0.20.3`). Distribution density visualizations were created using the Scott bandwidth density estimator [45], as implemented in the seaborn software package (`0.9.0`).

Higher-level statistical modelling was performed with the Statsmodels software package [46] (version `0.9.9`), and the SciPy software package [47] (version `1.1.0`). Model parameters were estimated using the ordinary least squares method, and a type 3 analysis of variance (ANOVA) was employed to control estimate variability for unbalanced categories. All t-tests producing explicitly noted p-values are two-tailed.

The VTA structural projection data used to compare and contrast the activation maps produced in this study was sourced from the Allen Brain Institute (ABI) mouse brain connectome dataset [48]. As the target promoter of this study (DAT) is not included in the ABI connectome study, all available promoters were used (Sty17, Erbb4, Slc6a3, Th, Cck, Pdzk1ip1, Chrna2, Hdc, Slc18a2, Calb2, and Rasgrf2). Datasets with left-handed VTA injection sides were flipped to provide right-hand VTA projection estimates. The data was converted and registered to the DSURQEC template space by the ABI Connectivity Data Generator package [49]. For the second-level statistical comparison between functional activation and structural projection, individual activation (betas) and projection maps were normalized to a common scale by subtracting the average and dividing by the standard deviation.

Software management relevant for the exact reproduction of the aforementioned environment was performed via neuroscience package install instructions for the Gentoo Linux distribution [50].

Reproducibility and Open Data

The resulting t-statistic maps (i.e. the top-level data visualized in this document), which document the opto-fMRI dopaminergic map in the mouse model, are distributed along the source-code of all analyses [51]. The BIDS [52] data archive which serves as the raw data recourse for this document is openly distributed [53], as is the full instruction set for recreating this document from the aforementioned raw data [51]. The source code for this document and all data analysis shown herein is structured according to the RepSeP specifications [54].

Results

For analysis, the various stimulation protocols tested are divided into two categories: block stimulation (where stimulation is delivered in continuous blocks of at least 8 s — tables S1 to S5) and phasic stimulation (encompassing protocols where stimulation is delivered in short bursts of up to 1 s in lenght — tables S6 and S7).

The VTA mean t statistic is found sensitive to the stimulation protocol category ($F_{1,54} = 41.79$, $p = 3.04 \times 10^{-8}$), the stimulation target depth ($F_{4,54} = 3.181$, $p = 0.02$), the stimulation target PA coordinates ($F_{3,54} = 3.196$, $p = 0.031$), but not the interaction of the depth and PA target coordinates ($F_{12,54} = 1.75$, $p = 0.12$).

The break-up by phasic and block stimulation is shown in fig. 2 and — accounting for the entire model, including target coordinates — both levels are significantly different from zero, with the phasic stimulation level of the variable yielding a p-value of 0.026, and the block stimulation level yielding a p-value of 0.00023. Upon an investigation of the t-statistic map, phasic stimulation, however, reveals no coherent activation pattern (fig. S3b).

The main and interaction effects of the implant coordinate variables are better described categorically than linearly (figs. S1 and 2b). Consequently, the most suitable implant coordinate group for the assay can best be determined based on a categorical classification of implant coordinates. We classify the implant coordinates into a "best" and a "rejected" group, by k-means clustering the aggregate VTA t-statistic scores into two clusters. This categorization is highlighted in fig. 2b.

For block stimulation, the best implant category group (fig. 3a) and the rejected implant category group (fig. 3c) show not only a difference in overall stimulus-evoked signal intensity, but also a difference in efferent distribution, with the rejected implant category efferent spectrum more strongly weighted towards caudal brain areas. This distinction specifically arises for implant categorization based on block scan VTA t-statistic means, and is not as salient if implants are categorized based on a posteroanterior implant coordinate delimiter (fig. S2).

The activation pattern elicited by block stimulation in the best implant category group shows strong coherent clusters of activation. The top activation areas are predominantly located in the right hemisphere, with the whole brain parcellation-resolved response showing highly significant laterality ($p = 1.89 \times 10^{-6}$). Activation is seen in regions surrounding the stimulation site, such as the ventral tegmental decussation and the interpeduncular nucleus. The largest activation cluster can be seen in the dopaminergic VTA projection areas, covering subcortical regions in the rostroventral region of the brain (nucleus accumbens, striatum, and the basal forebrain), while weaker activation was observed in smaller structures in the vicinity of the above regions, such as the fasciculus retroflexus, anterior commissure and the claustrum.

This activation pattern is is largely consistent with structural projection data, as published by the Allen Brain Institute [48] with a few notable distinctions (fig. 4). At the parcellation level, we see a moderately strong positive correlation between functional activation and structural projection (fig. 4a), which is weaker at the voxel level (fig. 4b). In the midbrain, the coronal slice map shows areas of increased functional activation with respect to structural projection in the contralateral VTA and the ipsilateral substantia nigra. Coherent areas of such activation are also observed in projection areas, most prominently in the ipsilateral and contralateral dorsomedial striatum (fig. 4c). Parcellation area distributions (figs. 4d and 4e), show the activation map encompassing additional areas of activation in the contralateral hemisphere (particularly the contralateral nucleus accumbens, with activity extending into the claustrum and anterior commissure region). The pattern of activation encompasses all regions with dense structural projections, with areas where structural projection overshoots functional activation being few and dispersed. These small clusters amount to weak negative contrast distributions in regions such as the cerebellum, the olfactory bulb, and the amygdaloid area (fig. 4d).

We differentiate VTA transmission from VTA excitability by mapping functional connectivity using a seed region in the right VTA, which yielded the projection pattern shown in fig. 3e. These clusters were more sparse compared to those identified by stimulus-evoked analysis, yet follow a similar distribution. While the top functional connectivity areas are located in the right hemisphere, the whole brain parcellation-resolved response displays no significant laterality ($p = 0.74$). Strong activation can be seen in the parcellation regions surrounding the seed, such as the ventral tegmental decussation and the closely located interpeduncular nucleus. Rostrovental dopaminergic projection areas remain prominently featured, including the nucleus accumbens and the striatum (fig. 3f).

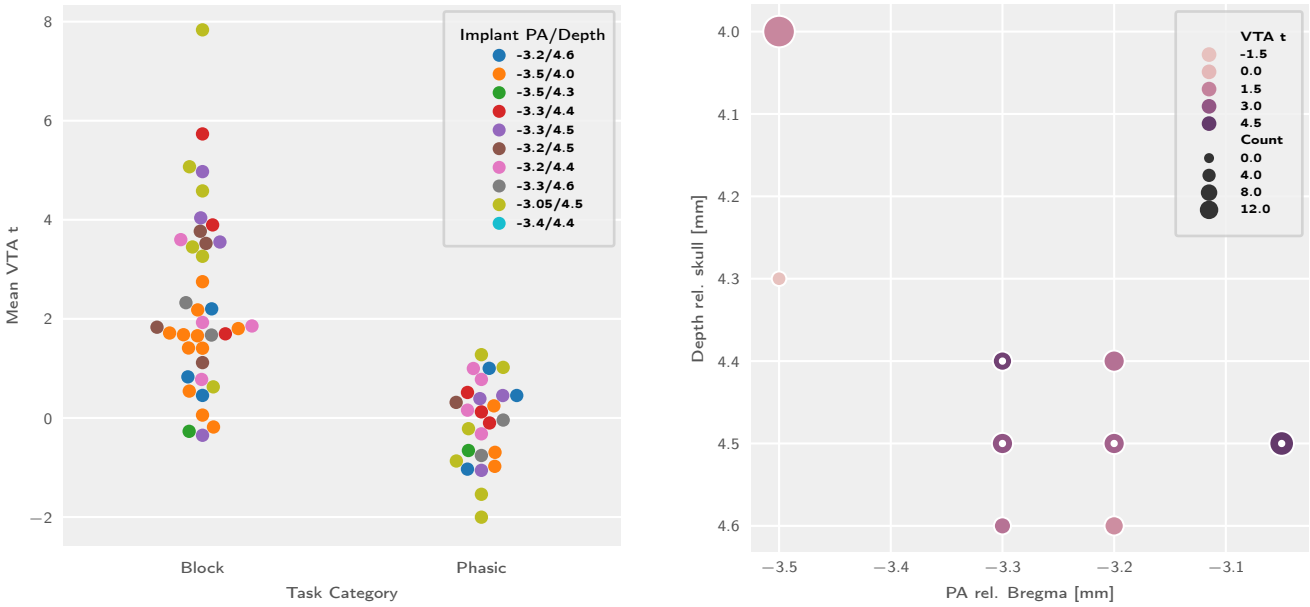

(a) Task group comparison for animals targeted at all explored combinations of implant coordinates.

(b) Implant coordinate comparison for block stimulation trials (inner dots indicate best category group).

Figure 2: VTA activation is sensitive to the stimulation protocol category and the implant coordinates, with different trends in block and phasic stimulation trials. Depicted are multifactorial (protocol and implant coordinates) comparisons of signal intensity in the VTA region of interest.

Stimulation in wild type control animals (which is corrected for in the aforementioned stimulus-evoked analyses) does not exhibit a pattern of activity consistent with dopaminergic projections. Sparse grains containing regression scores of $t \geq 3$ can be observed, with the largest cluster in the lateral geniculate nucleus area of the thalamus, suggesting visual activity (fig. S7b). Atlas parcellation score distributions (fig. S7c) do not strongly deviate from zero, with the highest score areas being in the vicinity of the fiber, which might indicate VTA heating artefacts (ventral tegmental decussation and the interpeduncular nucleus). Comparable region t-statistic distributions are also found in areas of the cerebellum (such as the dentate nucleus). Overall the whole brain parcellation-resolved response shows no significant laterality ($p = 0.87$).

Histological analysis of the targeting site reveals that the optic fiber implant displaces the YFP labelled neurons of the VTA (fig. 5). This dislocation was observed irrespective of the targeting area or the speed of implant insertion (10 to 50 µm/s). Higher magnification (fig. 5c) reveals, however, that labeled filaments and soma remain in the imediate vecinity of the fiber tip.

Discussion

Whole-Brain Dopaminergic Map

In this article we present the first whole-brain opto-fMRI map of VTA dopaminergic activity in the mouse. Published as voxelwise reusable data and discussed in terms of regions of interest in the article text, this constitutes an essential resource for model animal study of the dopaminergic system. The areas identified as functional VTA dopaminergic targets are largely consistent with histological and electrophysiologic literature (as summarized in fig. 1a). This highlights the suitability of opto-fMRI for interrogating the mouse dopaminergic system, in addition to such advantages as longitudinal recording capability and whole-brain coverage.

The predominant VTA projection area identified both in literature and in our study is the nucleus accumbens. This area is involved in numerous neuropsychological phenomena, and its activation further supports the method's suitability to resolve meaningful brain function and increase the predictability of novel interventions using the mouse model organism.

Throughout most brain regions, we observe a high degree of correspondence between functional activation and structural projection density. We do, however, also resolve a number of notable differences between opto-fMRI derived projection areas and the structural substrate of the dopaminergic system. Overall, the contrast between function and structure shows stronger signal and wider coverage for the functional activation pattern, particularly in projection areas. Notably, the functional map extends into the contralateral ventral striatum, and both the contralateral and ipsilateral dorsal striatum. The first of these features corresponds to an extension of the functional map to the contralateral VTA in the midbrain, and is further supported by the contralateral projection areas showing lower overall significance scores than the ipsilateral areas (figs. 3b and 3f). The explanation of projection area extension into the dorsal striatum on account of secondary activation of the ipsilateral substantia nigra is however less reliable, since the most relevant cluster of increased func-

tional activation — the dorsomedial striatum — can be observed bilaterally, though potential nigral activation is only seen ipsilaterally (fig. 4c). Not least of all, the local deformation of the VTA upon fiber implantation may confound parcellation in the vicinity of the fiber tip (fig. 5).

The distinction between the two pairs of dopaminergic nuclei and their two pathways — mesocorticolimbic (originating in the VTA and projecting into the ventral striatum) and nigrostriatal (originating in the substantia nigra and projecting into the dorsal striatum) — forms the basis for dopaminergic modelling. In this context, the dorsomedial striatum has received attention in conjunction with associative rather than sensorimotor function (which is commonly ascribed to the nigrostriatal pathway) [55, 56]. Together with other recent literature [57, 18], our results contribute to a body of evidence questioning the strict dichotomy of dopaminergic pathways, and suggesting that VTA activation may also functional responses in some projection areas commonly classified as nigrostriatal.

The amygdala, hippocampus, and the medial prefrontal cortex — known targets for VTA dopaminergic projections — do not reveal strong activation in opto-fMRI. Comparison with published structural projection data, however, indicates that this is due to low fiber bundle density, as these areas also do not show high amounts of structural projections. Partly negative t-statistic distributions of the contrast between functional activation and structural projection can be observed in areas adjacent to the amygdala (fig. 4d), though it should be noted that they are comparable to differences observed in the cerebellar white matter.

We also present a VTA seed-based connectivity analysis which attempts to differentiate primary activation from subsequent signal transmission (according to a simple 1-step signal relay model depicted in fig. 1b). Our results indicate that this analysis is capable of resolving projection areas, but is significantly less powerful than stimulus-evoked analysis (fig. 3a). VTA seed based analysis highlights only a small number of activation clusters and fails to show signal laterality. This is an interesting outcome, as — given the superior performance of stimulus-evoked analysis — it describes two possible features of dopaminergic neurotransmission in the VTA. The first is that the relay of primary VTA stimulation has higher fidelity than the fMRI measurement of VTA activity itself (i.e. VTA activity is relayed accurately, but outweighed by measurement noise). The second is that there is a significant threshold to dopaminergic neurotransmission, by which fMRI-measurable baseline activity is predominantly not propagated (i.e. VTA activity is measured accurately, but is relayed in a strongly filtered fashion).

Assay Parameters

In addition to describing the results of a novel assay, this article presents evidence-based suggestions for assay reuse and refinement. In particular, we detail the effects of stimulus protocol categories and optogenetic targeting coordinates on the performance of the method.

The optic stimulation target coordinate break-down in fig. 2 shows that, in block stimulation trials, more rostral and deeper implant coordinates elicit stronger VTA activity. Based on present data we recommend targeting the optic implant at a posteroanterior distance of $-3.05\,\mathrm{mm}$ from bregma, a left-right distance of 0.5 to $0.55\,\mathrm{mm}$ from the midline, and a depth of $4.5\,\mathrm{mm}$ from the skull surface. Additional coordinate exploration might be advisable, though further progression towards bregma may lead to direct stimulation of specific efferent fibers rather than the VTA.

The absence of strong VTA activation effects as well as coherent activity patterns elicited by phasic stimulation (figs. 2a and S3b) highlights that phasic stimulation is unable to elicit activation measurable by the assay in its current form. The overall low susceptibility to phasic stimulation is most likely due to the intrinsically lower statistical power of such stimulation protocols in fMRI, but might also reflect lower neuronal susceptibility to phasic stimulation. While this hypothesis is strongly speculative, we highlight that it is testable, and phasic stimulation should be revisited upon strong alterations to the measurement protocol or experiment design.

Regarding the distribution of activation across projection areas, we note a strong and unexpected divergence between the most sensitive ("best") and least sensitive ("rejected") implant coordinate category responses to block stimulation (figs. 3a and 3c). In addition to a difference in VTA and efferent signal intensity (expected as per the selection criterion), we also notice a different pattern of target areas. Interestingly, the activity pattern elicited in the "rejected" group is more strongly weighted towards the hindbrain, and the efferent pattern includes the periaqueductal gray, a prominent brainstem nucleus involved in emotional regulation [58]. This effect might be related to the activation of descending dopaminergic projections, though further investigation is needed to clarify this point and, in general, to better understand the cross-connectivity between deep brain nuclei.

The activation patterns in wild type control animals are narrow in their extent (fig. S7), and — when controlled for — do not meaningfully impact the dopaminergic block stimulation contrast (figs. 3a and S4). Based on the activation distribution, however, it may be inferred that trace heating artefacts (midbrain activation) and visual stimulation (lateral geniculate nucleus thalamic activation) are present. On account of this, for further experiments, we suggest using eye occlusion, dark or dark-painted ferrule sleeves, as well as laser intensities lower than the $30\,\mathrm{mW}$ ($239\,\mathrm{mW/mm^2}$) used in this study.

While stimulus-evoked analysis displayed significant laterality, large clusters of significant activation were also observed on the contralateral side. Fluorescence microscopy (fig. 4c) revealed that the expression of the

viral construct injected at the site of the right VTA extends over a large area, that encompasses the contralateral VTA. Inspection of the functional map at the midbrain stimulation site corroborates that activity in fact spreads to the contralateral VTA (fig. 3a). This explains the occurrence of contralateral fMRI responses, which are most likely weaker due to a lower photon fluence at the site of the left VTA. Together, these data suggest that the virus amount injected for the assay could be significantly reduced, to less than the 0.4 µl (5.7×10^{12} vg/ml) used as the minimal volume in this study.

Lastly, the most salient qualitative feature of fig. 5 is the displacement of labelled neurons from the area in the proximity of the optic fiber implant tip. This feature was consistent across animals and implantation sites, and is cause for concern, since it limits the extent to which cells can be optically stimulated. Particularly, such a feature could exacerbate limitations arising from heating artefacts, since the maximum SNR attainable at a particular level of photon fluence may be capped to an unnecessarily low level. This effect might be mitigated by using thinner optic fiber implants (e.g. ⌀200 µm, as opposed to the ⌀400 µm fibers used in this study).

Conclusion

In this article we present the first whole-brain map of VTA dopaminergic signalling in the mouse, and publish it in a standard space aligned with stereotactic manipulation coordinates [51]. We determine that the mapping is consistent with known structural projections, and note the instances where differences are observed. Further, we explore network structure aware analysis via functional connectivity, finding that the assay provides limited support for signal relay imaging. As part of this work we perform an in-depth investigation of experimental variation, and summarize evidence-based instructions for assay reuse. The results herein published provide a reference dopaminergic stimulus-evoked functional neurophenotype map and a novel and thoroughly documented workflow for the preclinical imaging of dopaminergic function, both of which are crucial to elucidating the etiology of numerous disorders and improving psychopharmacological interventions in health and disease.

References

[1] Matthew W Rice, Rosalinda C Roberts, Miguel Melendez-Ferro, and Emma Perez-Costas. Mapping dopaminergic deficiencies in the substantia nigra/ventral tegmental area in schizophrenia. *Brain Structure and Function*, 221(1):185–201, January 2016. doi: 10.1007/s00429-014-0901-y.

[2] Dwight C German and Kebreten F Manaye. Midbrain dopaminergic neurons (nuclei a8, a9, and a10): three-dimensional reconstruction in the rat. *Journal of Comparative Neurology*, 331(3):297–309, May 1993. doi: 10.1002/cne.903310302.

[3] LC Triarhou, J Norton, and Bernardino Ghetti. Mesencephalic dopamine cell deficit involves areas a8, a9 and a10 in weaver mutant mice. *Experimental brain research*, 70(2):256–265, April 1988. doi: 10.1007/BF00248351.

[4] G. Di Chiara and A. Imperato. Drugs abused by humans preferentially increase synaptic dopamine concentrations in the mesolimbic system of freely moving rats. *Proceedings of the National Academy of Sciences*, 85(14):5274–5278, July 1988. doi: 10.1073/pnas.85.14.5274. URL `https://doi.org/10.1073/pnas.85.14.5274`.

[5] Gaetano Di Chiara. Drug addiction as dopamine-dependent associative learning disorder. *European Journal of Pharmacology*, 375(1-3):13–30, June 1999. doi: 10.1016/s0014-2999(99)00372-6. URL `https://doi.org/10.1016/s0014-2999(99)00372-6`.

[6] A Nieoullon. Dopamine and the regulation of cognition and attention. *Progress in Neurobiology*, 67(1):53–83, May 2002. doi: 10.1016/s0301-0082(02)00011-4. URL `https://doi.org/10.1016/s0301-0082(02)00011-4`.

[7] John D. Salamone. The involvement of nucleus accumbens dopamine in appetitive and aversive motivation. *Behavioural Brain Research*, 61(2):117–133, April 1994. doi: 10.1016/0166-4328(94)90153-8. URL `https://doi.org/10.1016/0166-4328(94)90153-8`.

[8] Soghra Akbari Chermahini and Bernhard Hommel. The (b)link between creativity and dopamine: Spontaneous eye blink rates predict and dissociate divergent and convergent thinking. *Cognition*, 115(3):458–465, June 2010. doi: 10.1016/j.cognition.2010.03.007. URL `https://doi.org/10.1016/j.cognition.2010.03.007`.

[9] Richard A. Depue and Paul F. Collins. Neurobiology of the structure of personality: Dopamine, facilitation of incentive motivation, and extraversion. *Behavioral and Brain Sciences*, 22(3):491–517, June 1999. doi: 10.1017/s0140525x99002046. URL `https://doi.org/10.1017/s0140525x99002046`.

[10] E. Masliah. Dopaminergic loss and inclusion body formation in -synuclein mice: Implications for neurodegenerative disorders. *Science*, 287(5456):1265–1269, February 2000. doi: 10.1126/science.287.5456.1265. URL `https://doi.org/10.1126/science.287.5456.1265`.

[11] O. D. Howes and S. Kapur. The dopamine hypothesis of schizophrenia: Version III–the final common pathway. *Schizophrenia Bulletin*, 35(3):549–562, March 2009. doi: 10.1093/schbul/sbp006. URL https://doi.org/10.1093/schbul/sbp006.

[12] Mitul A. Mehta, Adrian M. Owen, Barbara J. Sahakian, Nahal Mavaddat, John D. Pickard, and Trevor W. Robbins. Methylphenidate enhances working memory by modulating discrete frontal and parietal lobe regions in the human brain. *The Journal of Neuroscience*, 20(6):RC65–RC65, March 2000. doi: 10.1523/jneurosci.20-06-j0004.2000. URL https://doi.org/10.1523/jneurosci.20-06-j0004.2000.

[13] Danielle C. Turner, Trevor W. Robbins, Luke Clark, Adam R. Aron, Jonathan Dowson, and Barbara J. Sahakian. Cognitive enhancing effects of modafinil in healthy volunteers. *Psychopharmacology*, 165(3):260–269, January 2003. ISSN 1432-2072. doi: 10.1007/s00213-002-1250-8. URL https://doi.org/10.1007/s00213-002-1250-8.

[14] Ana Aransay, Claudia Rodríguez-López, María García-Amado, Francisco Clascá, and Lucía Prensa. Long-range projection neurons of the mouse ventral tegmental area: a single-cell axon tracing analysis. *Frontiers in Neuroanatomy*, 9, May 2015. doi: 10.3389/fnana.2015.00059. URL https://doi.org/10.3389/fnana.2015.00059.

[15] Howard L. Fields, Gregory O. Hjelmstad, Elyssa B. Margolis, and Saleem M. Nicola. Ventral tegmental area neurons in learned appetitive behavior and positive reinforcement. *Annual Review of Neuroscience*, 30(1):289–316, July 2007. doi: 10.1146/annurev.neuro.30.051606.094341. URL https://doi.org/10.1146/annurev.neuro.30.051606.094341.

[16] Satoshi Ikemoto. Dopamine reward circuitry: Two projection systems from the ventral midbrain to the nucleus accumbens–olfactory tubercle complex. *Brain Research Reviews*, 56(1):27–78, November 2007. doi: 10.1016/j.brainresrev.2007.05.004. URL https://doi.org/10.1016/j.brainresrev.2007.05.004.

[17] T. S. Hnasko, G. O. Hjelmstad, H. L. Fields, and R. H. Edwards. Ventral tegmental area glutamate neurons: Electrophysiological properties and projections. *Journal of Neuroscience*, 32(43):15076–15085, October 2012. doi: 10.1523/jneurosci.3128-12.2012. URL https://doi.org/10.1523/jneurosci.3128-12.2012.

[18] Weixing X. Pan, Tianyi Mao, and Joshua T. Dudman. Inputs to the dorsal striatum of the mouse reflect the parallel circuit architecture of the forebrain. *Frontiers in Neuroanatomy*, 4, December 2010. doi: 10.3389/fnana.2010.00147. URL https://doi.org/10.3389/fnana.2010.00147.

[19] Gonzalo E. Torres, Raul R. Gainetdinov, and Marc G. Caron. Plasma membrane monoamine transporters: structure, regulation and function. *Nature Reviews Neuroscience*, 4(1):13–25, January 2003. doi: 10.1038/nrn1008. URL https://doi.org/10.1038/nrn1008.

[20] Kei Yamamoto and Philippe Vernier. The evolution of dopamine systems in chordates. *Frontiers in Neuroanatomy*, 5, March 2011. doi: 10.3389/fnana.2011.00021. URL https://doi.org/10.3389/fnana.2011.00021.

[21] Seth R. Taylor, Sylvia Badurek, Ralph J. Dileone, Raad Nashmi, Liliana Minichiello, and Marina R. Picciotto. GABAergic and glutamatergic efferents of the mouse ventral tegmental area. *Journal of Comparative Neurology*, 522(14):3308–3334, July 2014. doi: 10.1002/cne.23603. URL https://doi.org/10.1002/cne.23603.

[22] Edward S Boyden, Feng Zhang, Ernst Bamberg, Georg Nagel, and Karl Deisseroth. Millisecond-timescale, genetically targeted optical control of neural activity. *Nature Neuroscience*, 8(9):1263–1268, August 2005. doi: 10.1038/nn1525. URL https://doi.org/10.1038/nn1525.

[23] P. C. Orban, D. Chui, and J. D. Marth. Tissue- and site-specific DNA recombination in transgenic mice. *Proceedings of the National Academy of Sciences*, 89(15):6861–6865, August 1992. doi: 10.1073/pnas.89.15.6861. URL https://doi.org/10.1073/pnas.89.15.6861.

[24] M. Desai, I. Kahn, U. Knoblich, J. Bernstein, H. Atallah, A. Yang, N. Kopell, R. L. Buckner, A. M. Graybiel, C. I. Moore, and E. S. Boyden. Mapping brain networks in awake mice using combined optical neural control and fMRI. *Journal of Neurophysiology*, 105(3):1393–1405, March 2011. doi: 10.1152/jn.00828.2010. URL https://doi.org/10.1152/jn.00828.2010.

[25] Joanes Grandjean, Alberto Corcoba, Martin C. Kahn, A. Louise Upton, Evan S. Deneris, Erich Seifritz, Fritjof Helmchen, Edward O. Mann, Markus Rudin, and Bechara J. Saab. A brain-wide functional map of the serotonergic responses to acute stress and fluoxetine. *Nature Communications*, 10(1), January 2019. doi: 10.1038/s41467-018-08256-w. URL https://doi.org/10.1038/s41467-018-08256-w.

[26] K.J. Friston, C.D. Frith, R. Turner, and R.S.J. Frackowiak. Characterizing evoked hemodynamics with fMRI. *NeuroImage*, 2(2):157–165, June 1995. doi: 10.1006/nimg.1995.1018. URL https://doi.org/10.1006/nimg.1995.1018.

[27] Xiaoxi Zhuang, Justine Masson, Jay A. Gingrich, Stephen Rayport, and René Hen. Targeted gene expression in dopamine and serotonin neurons of the mouse brain. *Journal of Neuroscience Methods*, 143(1):27–32, April 2005. doi: 10.1016/j.jneumeth.2004.09.020. URL https://doi.org/10.1016/j.jneumeth.2004.09.020.

[28] Florian Aymanns, Markus Rudin, and Horea-Ioan Ioanas. COSplay: Contrast optimized stimulation player. *Journal of Open Source Software*, 4(39):1171, July 2019. doi: 10.21105/joss.01171. URL https://doi.org/10.21105/joss.01171.

[29] Horea-Ioan Ioanas, Bechara Saab, and Markus Rudin. LabbookDB: A wet-work-tracking database application framework. *Proceedings of the 16th Python in Science Conference*, July 2017. doi: 10.25080/shinma-7f4c6e7-004. URL https://doi.org/10.25080/shinma-7f4c6e7-004.

[30] Joanes Grandjean, Aileen Schroeter, Imene Batata, and Markus Rudin. Optimization of anesthesia protocol for resting-state fmri in mice based on differential effects of anesthetics on functional connectivity patterns. *NeuroImage*, 102 Pt 2:838–847, November 2014. ISSN 1095-9572. doi: 10.1016/j.neuroimage.2014.08.043.

[31] Horea-Ioan Ioanas, Markus Marks, Clément M. Garin, Marc Dhenain, Mehmet Fatih Yanik, and Markus Rudin. An automated open-source workflow for standards-compliant integration of small animal magnetic resonance imaging data. June 2019. doi: 10.1101/667980. URL https://doi.org/10.1101/667980.

[32] Horea-Ioan Ioanas, Markus Marks, Tina Segessemann, Dominik Schmidt, Florian Aymanns, and Markus Rudin. SAMRI — Small Animal Magnetic Resonance Imaging, January 2019. URL https://doi.org/10.5281/zenodo.3234918.

[33] Horea-Ioan Ioanas, Markus Marks, Mehmet Fatih Yanik, and Markus Rudin. An optimized registration workflow and standard geometric space for small animal brain imaging. *bioRxiv*, 2019. doi: 10.1101/619650. URL https://www.biorxiv.org/content/early/2019/04/26/619650.

[34] Brian B. Avants, Nicholas J. Tustison, Gang Song, Philip A. Cook, Arno Klein, and James C. Gee. A reproducible evaluation of ANTs similarity metric performance in brain image registration. *NeuroImage*, 54(3):2033–2044, February 2011. doi: 10.1016/j.neuroimage.2010.09.025. URL https://doi.org/10.1016/j.neuroimage.2010.09.025.

[35] Horea-Ioan Ioanas, Tina Segessemann, and Markus Rudin. "Mouse Brain Atlases" generator workflows, January 2019. URL https://doi.org/10.5281/zenodo.2545838.

[36] A.E. Dorr, J.P. Lerch, S. Spring, N. Kabani, and R.M. Henkelman. High resolution three-dimensional brain atlas using an average magnetic resonance image of 40 adult c57bl/6j mice. *NeuroImage*, 42(1):60–69, August 2008. doi: 10.1016/j.neuroimage.2008.03.037. URL https://doi.org/10.1016/j.neuroimage.2008.03.037.

[37] Robert W Cox. AFNI: software for analysis and visualization of functional magnetic resonance neuroimages. *Computers and Biomedical research*, 29(3):162–173, June 1996. doi: 10.1006/cbmr.1996.0014. URL https://www.sciencedirect.com/science/article/pii/S0010480996900142.

[38] Mark Jenkinson, Christian F. Beckmann, Timothy E J. Behrens, Mark W. Woolrich, and Stephen M. Smith. FSL. *Neuroimage*, 62(2):782–790, August 2012. doi: 10.1016/j.neuroimage.2011.09.015. URL http://dx.doi.org/10.1016/j.neuroimage.2011.09.015.

[39] Patrick E. Steadman, Jacob Ellegood, Kamila U. Szulc, Daniel H. Turnbull, Alexandra L. Joyner, R. Mark Henkelman, and Jason P. Lerch. Genetic effects on cerebellar structure across mouse models of autism using a magnetic resonance imaging atlas. *Autism Research*, 7(1):124–137, October 2013. doi: 10.1002/aur.1344. URL https://doi.org/10.1002/aur.1344.

[40] Jeremy F.P. Ullmann, Charles Watson, Andrew L. Janke, Nyoman D. Kurniawan, and David C. Reutens. A segmentation protocol and MRI atlas of the c57bl/6j mouse neocortex. *NeuroImage*, 78:196–203, September 2013. doi: 10.1016/j.neuroimage.2013.04.008. URL https://doi.org/10.1016/j.neuroimage.2013.04.008.

[41] Kay Richards, Charles Watson, Rachel F. Buckley, Nyoman D. Kurniawan, Zhengyi Yang, Marianne D. Keller, Richard Beare, Perry F. Bartlett, Gary F. Egan, Graham J. Galloway, George Paxinos, Steven Petrou, and David C. Reutens. Segmentation of the mouse hippocampal formation in magnetic resonance images. *NeuroImage*, 58(3):732–740, October 2011. doi: 10.1016/j.neuroimage.2011.06.025. URL https://doi.org/10.1016/j.neuroimage.2011.06.025.

[42] Matthew Brett, Michael Hanke, Chris Markiewicz, Marc-Alexandre Côté, Paul McCarthy, Chris Cheng, Yaroslav Halchenko, Satrajit Ghosh, Demian Wassermann, Stephan Gerhard, Eric Larson, Gregory R. Lee, Erik Kastman, Cindee M, Félix C. Morency, moloney, Ariel Rokem, Michiel Cottaar, Jarrod Millman, Ross Markello, jaeilepp, Alexandre Gramfort, Robert D Vincent, Jasper J.F. van den Bosch, Krish Subramaniam, Pradeep Reddy Raamana, Mathias Goncalves, Nolan Nichols, embaker, and Basile. nipy/nibabel: 2.3.1, October 2018. URL https://doi.org/10.5281/zenodo.1464282.

[43] Alexandre Abraham, Fabian Pedregosa, Michael Eickenberg, Philippe Gervais, Andreas Mueller, Jean Kossaifi, Alexandre Gramfort, Bertrand Thirion, and Gaël Varoquaux. Machine learning for neuroimaging with scikit-learn. *Frontiers in Neuroinformatics*, 8, February 2014. doi: 10.3389/fninf.2014.00014. URL https://doi.org/10.3389/fninf.2014.00014.

[44] F. Pedregosa, G. Varoquaux, A. Gramfort, V. Michel, B. Thirion, O. Grisel, M. Blondel, P. Prettenhofer, R. Weiss, V. Dubourg, J. Vanderplas, A. Passos, D. Cournapeau, M. Brucher, M. Perrot, and E. Duchesnay. Scikit-learn: Machine learning in Python. *Journal of Machine Learning Research*, 12:2825–2830, October 2011.

[45] David W. Scott. On optimal and data-based histograms. *Biometrika*, 66(3):605–610, December 1979. doi: 10.1093/biomet/66.3.605. URL https://doi.org/10.1093/biomet/66.3.605.

[46] Skipper Seabold and Josef Perktold. Statsmodels: Econometric and statistical modeling with Python. In *9th Python in Science Conference*, June 2010. URL http://conference.scipy.org/proceedings/scipy2010/pdfs/seabold.pdf.

[47] Travis E. Oliphant. Python for scientific computing. *Computing in Science & Engineering*, 9(3):10–20, June 2007. doi: 10.1109/mcse.2007.58. URL https://doi.org/10.1109/mcse.2007.58.

[48] Seung Wook Oh, Julie A Harris, Lydia Ng, Brent Winslow, Nicholas Cain, Stefan Mihalas, Quanxin Wang, Chris Lau, Leonard Kuan, Alex M Henry, et al. A mesoscale connectome of the mouse brain. *Nature*, 508(7495):207, April 2014. doi: 10.1038/nature13186. URL http://www.neuro-s.co.jp/images/product/5-151/5-1515.pdf.

[49] Tina Segessemann, Markus Rudin, and Horea-Ioan Ioanas. Abi connectivity data package generator, October 2019. URL https://doi.org/10.5281/zenodo.3523375.

[50] Horea-Ioan Ioanas, Bechara Saab, and Markus Rudin. Gentoo linux for neuroscience - a replicable, flexible, scalable, rolling-release environment that provides direct access to development software. *Research Ideas and Outcomes*, 3:e12095, February 2017. doi: 10.3897/rio.3.e12095. URL https://doi.org/10.3897/rio.3.e12095.

[51] Horea-Ioan Ioanas, Bechara John Saab, and Markus Rudin. Source Code for "A Whole-Brain Map and Assay Parameter Analysis of Mouse VTA Dopaminergic Activation", June 2019. URL https://doi.org/10.5281/zenodo.3263779.

[52] Krzysztof J Gorgolewski, Tibor Auer, Vince D Calhoun, R Cameron Craddock, Samir Das, Eugene P Duff, Guillaume Flandin, Satrajit S Ghosh, Tristan Glatard, Yaroslav O Halchenko, et al. The brain imaging data structure, a format for organizing and describing outputs of neuroimaging experiments. *Scientific Data*, 3:160044, June 2016. doi: 10.1038/sdata.2016.44. URL https://doi.org/10.1038/sdata.2016.44.

[53] Horea-Ioan Ioanas, Bechara John Saab, and Markus Rudin. BIDS Data for "A Whole-Brain Map and Assay Parameter Analysis of Mouse VTA Dopaminergic Activation", June 2019. URL https://doi.org/10.5281/zenodo.3236930.

[54] Horea-Ioan Ioanas and Markus Rudin. Reproducible self-publishing for Python-based research. EuroSciPy, August 2018. doi: 10.6084/m9.figshare.7247339.v1. URL https://figshare.com/articles/Reproducible_Self-Publishing_for_Python-Based_Research/7247339.

[55] Mimi Liljeholm and John P. O'Doherty. Contributions of the striatum to learning, motivation, and performance: an associative account. *Trends in Cognitive Sciences*, 16(9):467–475, September 2012. doi: 10.1016/j.tics.2012.07.007. URL https://doi.org/10.1016/j.tics.2012.07.007.

[56] Henry H. Yin, Sean B. Ostlund, Barbara J. Knowlton, and Bernard W. Balleine. The role of the dorsomedial striatum in instrumental conditioning. *European Journal of Neuroscience*, 22(2):513–523, July 2005. doi: 10.1111/j.1460-9568.2005.04218.x. URL https://doi.org/10.1111/j.1460-9568.2005.04218.x.

[57] S Lohani, A J Poplawsky, S-G Kim, and B Moghaddam. Unexpected global impact of VTA dopamine neuron activation as measured by opto-fMRI. *Molecular Psychiatry*, 22(4):585–594, July 2016. doi: 10.1038/mp.2016.102. URL https://doi.org/10.1038/mp.2016.102.

[58] E. E. Benarroch. Periaqueductal gray: An interface for behavioral control. *Neurology*, 78(3):210–217, January 2012. doi: 10.1212/wnl.0b013e31823fcdee. URL https://doi.org/10.1212/wnl.0b013e31823fcdee.

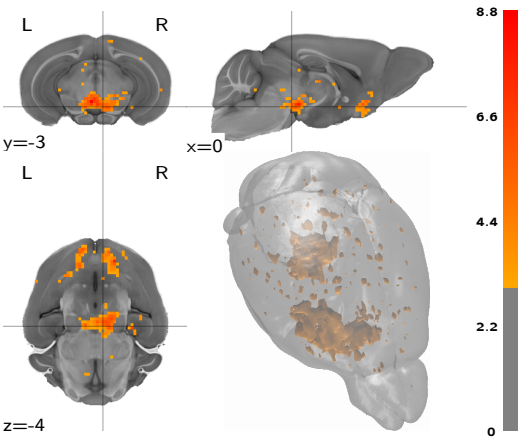

(a) Second-level t-statistic map for block-stimulus-evoked activity in best implant group animals (corrected for the wild type control response).

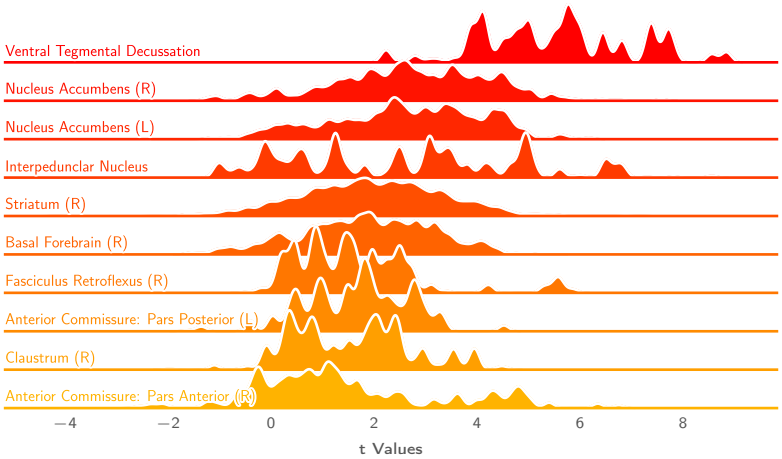

(b) Distribution densities of statistic values from block-stimulus-evoked activity analysis in best implant group animals (corrected for the wildtype control response). Depicted are the 10 most strongly activated areas.

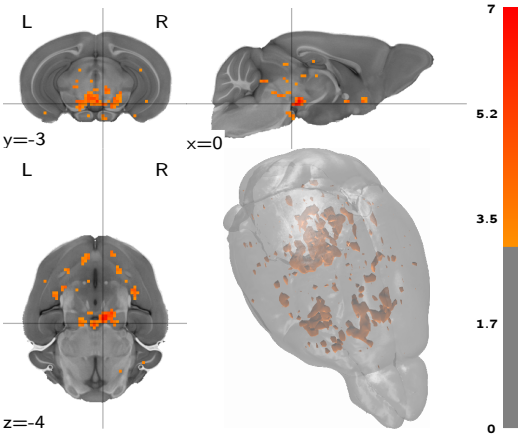

(c) Second-level t-statistic map for block-stimulus-evoked activity in rejected implant group animals (corrected for the wild type control response).

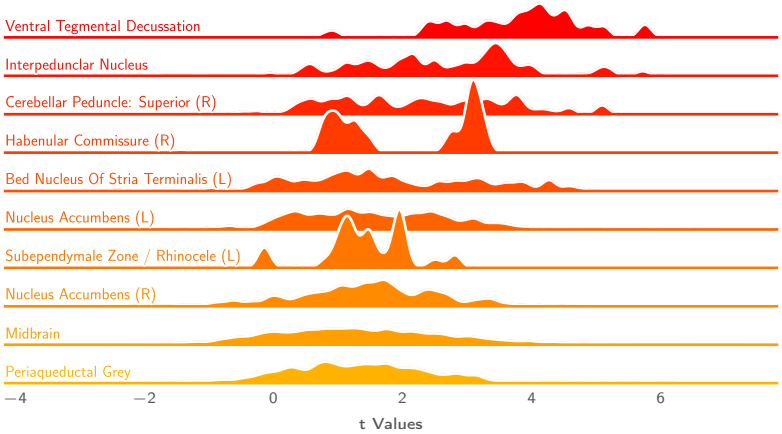

(d) Distribution densities of statistic values from block-stimulus-evoked activity analysis in rejected implant group animals (corrected for the wild type control response). Depicted are the 10 most strongly activated areas.

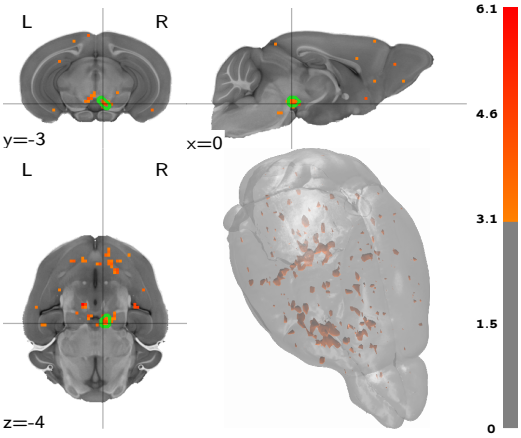

(e) Second-level t-statistic map for VTA seed-based functional connectivity during block stimulation in best implant group animals (VTA region in green).

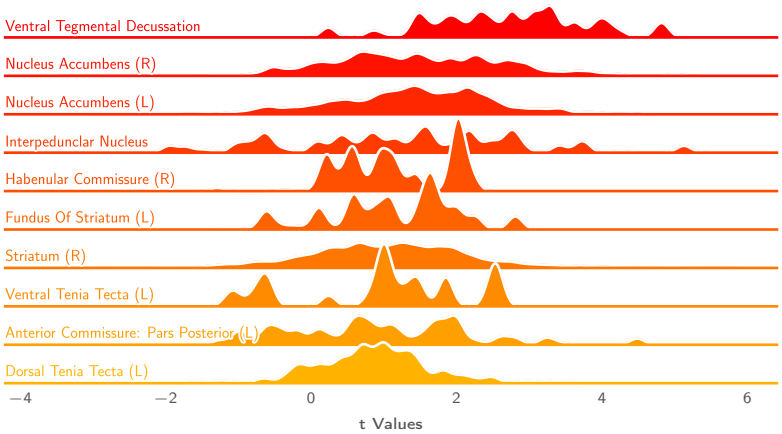

(f) Distribution densities of statistic values from seed-based functional connectivity analysis of best implant group animal block stimulation scans. Depicted are the 10 most strongly activated areas.

Figure 3: Block stimulation elicits strong ventral striatal activity in the best implant group, more rostrally weighted activity in the rejected implant group, and generates similar but weaker contrasts for VTA seed-based analysis. The figures show volumetric population t-statistic maps **(a, e, c)** thresholded at $t \geq 3$ and centered on the VTA target, as well as a break-down of activation along atlas parcellation regions **(b, d, f)**.

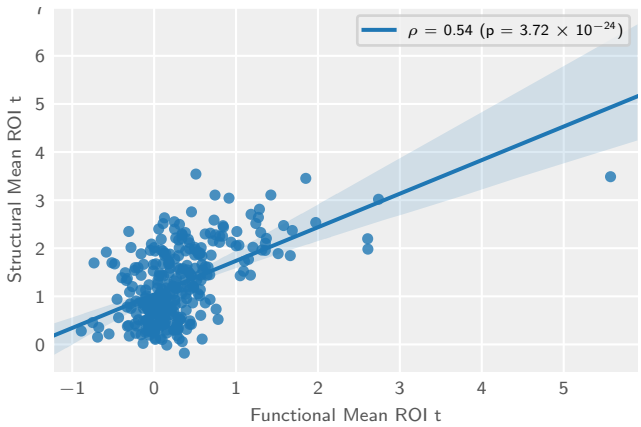

(a) Region-wise regression plot between functional and structural projection maps. Tinted area indicates the 99 % confidence interval of the regression estimate.

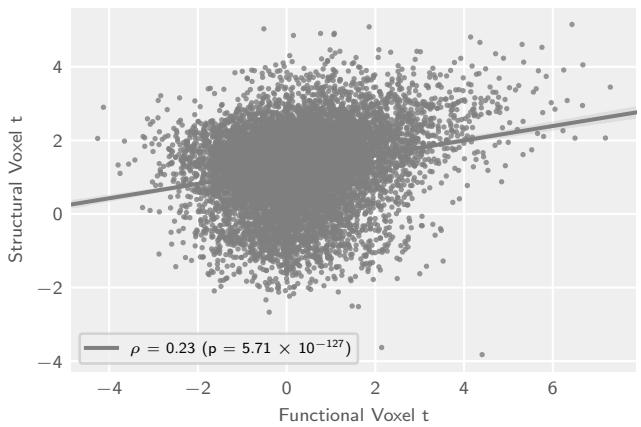

(b) Voxel-wise regression plot between functional and structural projection maps. Tinted area indicates the 99 % confidence interval of the regression estimate.

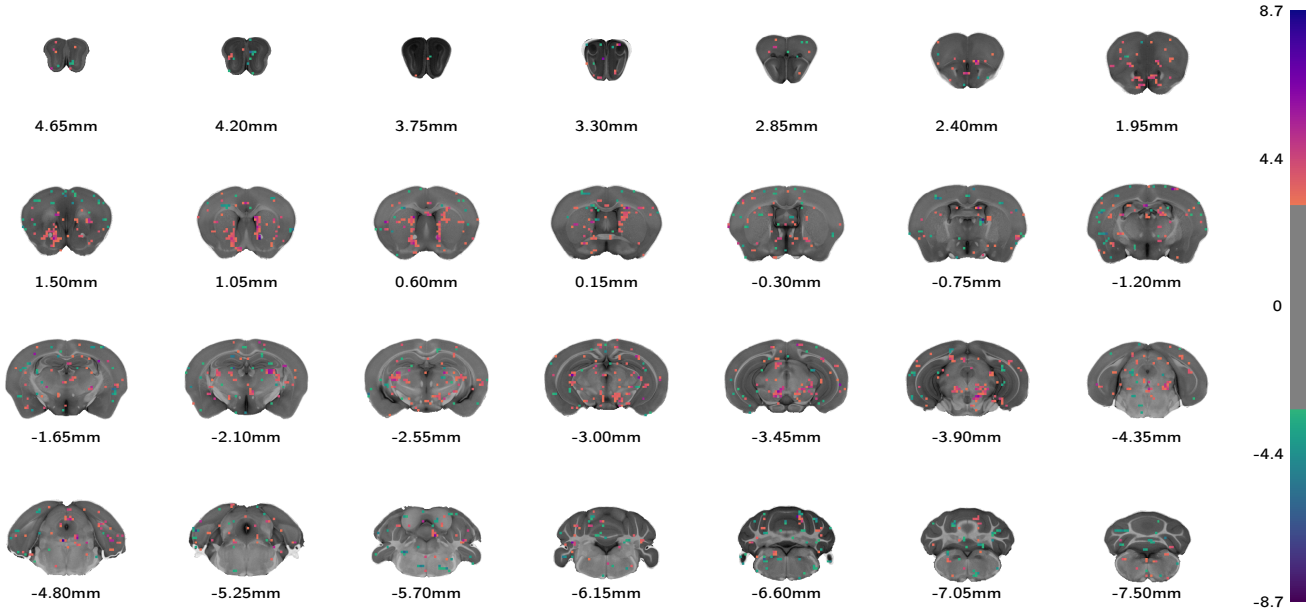

(c) Coronal slices, showing the population-level contrast t-statistic between VTA functional activation and VTA structural projections.

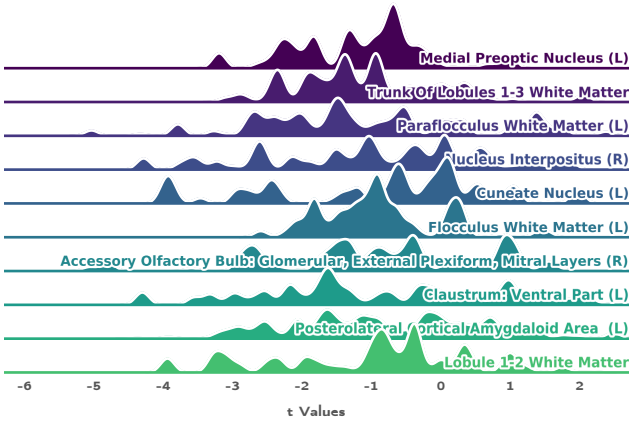

(d) Distribution densities of t-statistics, showing the regions where VTA structural projection exceeds functional activation most strongly.

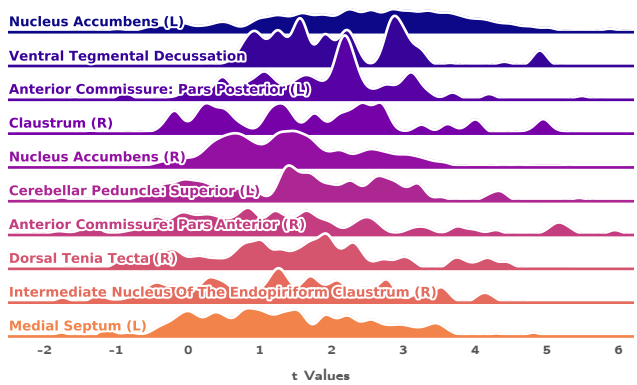

(e) Distribution densities of t-statistics, showing the regions where VTA functional activation exceeds structural projection most strongly.

Figure 4: Comparing VTA functional activation to structural projection data reveals good correspondence, with deviations involving the dorsomedial striatum and the contralateral ventral striatum. Depicted are correlation analyses **(a, b)** of the population-level functional and structural statistic scores, alongside statistic distributions **(c, d, e)** for the contrast, taking into account variability across subjects.

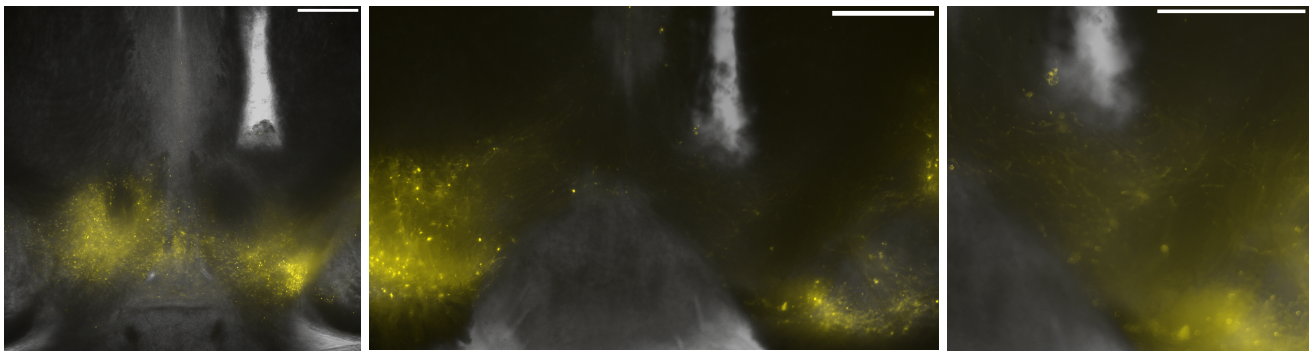

(a) 3.05 mm caudal of Bregma. **(b)** 3.5 mm caudal of Bregma. **(c)** 3.5 mm caudal of Bregma.

Figure 5: Fiber implantation causes strong local cell displacement in the VTA. Depicted are YFP (coexpressed with Channelrhodopsin) fluorescent microscopy images of the VTA, overlaid on corresponding transmission microscopy images of the same focal plane. All slices are seen in neurological orientation (the right of the image corresponds to the right of the animal). A higher magnification of **(b)** is depicted in **(c)**. White bars indicate a scale of 500 µm, and slices are shown in neurological orientation.

Supplementary Materials

Onset [s]	Duration [s]	Frequency [Hz]	Pulse Width [s]
182.0	20.0	20.0	0.005
332.0	20.0	20.0	0.005
482.0	20.0	20.0	0.005
632.0	20.0	20.0	0.005
782.0	20.0	20.0	0.005
932.0	20.0	20.0	0.005
1082.0	20.0	20.0	0.005
1232.0	20.0	20.0	0.005

Table S1: Block stimulation protocol, coded "CogB".

Onset [s]	Duration [s]	Frequency [Hz]	Pulse Width [s]
180.0	20.0	20.0	0.005
310.0	20.0	20.0	0.005
480.0	20.0	20.0	0.005
630.0	20.0	20.0	0.005
780.0	20.0	20.0	0.005
930.0	20.0	20.0	0.005
1080.0	20.0	20.0	0.005
1230.0	20.0	20.0	0.005

Table S2: Block stimulation protocol, coded "CogBr".

Onset [s]	Duration [s]	Frequency [Hz]	Pulse Width [s]
192.0	30.0	20.0	0.005
342.0	30.0	20.0	0.005
492.0	30.0	20.0	0.005
642.0	30.0	20.0	0.005
792.0	30.0	20.0	0.005
942.0	30.0	20.0	0.005
1092.0	30.0	20.0	0.005
1242.0	30.0	20.0	0.005

Table S3: Block stimulation protocol, coded "CogBl".

Onset [s]	Duration [s]	Frequency [Hz]	Pulse Width [s]
180.0	8.0	20.0	0.005
330.0	10.0	20.0	0.005
480.0	12.0	20.0	0.005
630.0	14.0	20.0	0.005
780.0	16.0	20.0	0.005
930.0	28.0	20.0	0.005
1080.0	20.0	20.0	0.005
1230.0	22.0	20.0	0.005

Table S4: Block stimulation protocol, coded "CogBm".

Onset [s]	Duration [s]	Frequency [Hz]	Pulse Width [s]
150.0000	20.0	15.0	0.005
280.0000	20.0	25.0	0.005
410.0000	20.0	15.0	0.010
540.0000	20.0	25.0	0.010
670.0000	20.0	15.0	0.005
799.9999	20.0	25.0	0.005
930.0000	20.0	15.0	0.010
1060.0000	20.0	25.0	0.010
1190.0000	20.0	15.0	0.005
1320.0000	20.0	25.0	0.005
1450.0000	20.0	15.0	0.010
1580.0000	20.0	25.0	0.010

Table S5: Block stimulation protocol, coded "CogMwf".

Onset [s]	Duration [s]	Frequency [Hz]	Pulse Width [s]
190.0	0.8	25.0	0.005
192.0	0.8	25.0	0.005
194.0	0.8	25.0	0.005
196.0	0.8	25.0	0.005
290.0	0.8	25.0	0.005
292.0	0.8	25.0	0.005
294.0	0.8	25.0	0.005
296.0	0.8	25.0	0.005
390.0	0.8	25.0	0.005
392.0	0.8	25.0	0.005
394.0	0.8	25.0	0.005
396.0	0.8	25.0	0.005
490.0	0.8	25.0	0.005
492.0	0.8	25.0	0.005
494.0	0.8	25.0	0.005
496.0	0.8	25.0	0.005
590.0	0.8	25.0	0.005
592.0	0.8	25.0	0.005
594.0	0.8	25.0	0.005
596.0	0.8	25.0	0.005

Table S6: Phasic stimulation protocol, coded "CogP".

Onset [s]	Duration [s]	Frequency [Hz]	Pulse Width [s]
50.0	1.0	20.0	0.005
90.0	1.0	20.0	0.005
130.0	1.0	20.0	0.005
170.0	1.0	20.0	0.005
210.0	1.0	20.0	0.005
250.0	1.0	20.0	0.005
290.0	1.0	20.0	0.005
330.0	1.0	20.0	0.005
370.0	1.0	20.0	0.005
410.0	1.0	20.0	0.005
450.0	1.0	20.0	0.005
490.0	1.0	20.0	0.005
530.0	1.0	20.0	0.005
570.0	1.0	20.0	0.005
610.0	1.0	20.0	0.005

Table S7: Phasic stimulation protocol, coded "JPogP".

In a linear modelling of the implant coordinate variables, the VTA mean t statistic is found sensitive only to the stimulation protocol category ($F_{1,59} = 51.04$, $p = 1.54 \times 10^{-9}$), but not the stimulation target depth ($F_{1,59} = 2.013$, $p = 0.16$), the stimulation target posteroanterior (PA) coordinates ($F_{1,59} = 2.229$, $p = 0.14$), and the interaction of the depth and PA target coordinates ($F_{1,59} = 1.98$, $p = 0.16$).

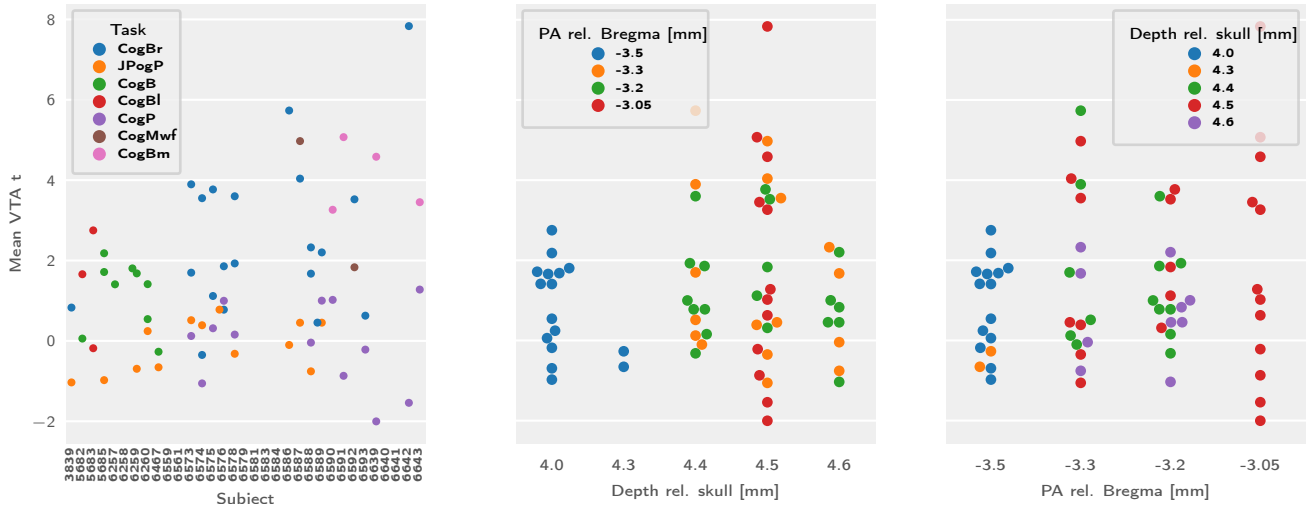

Figure S1: Multifactorial (depth and posteroantior) implant coordinate comparisons of signal intensity in the VTA region of interest. Protocols coded as in tables S1 to S7.

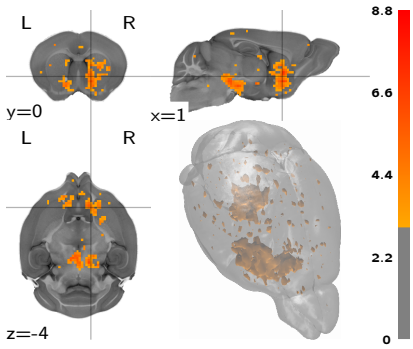

(a) Block stimulation of best implant category group (according to VTA activation), centered on largest cluster.

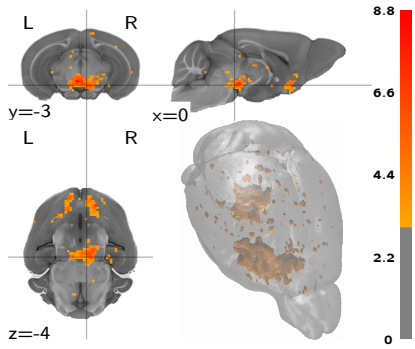

(b) Block stimulation of rejected implant category group (according to VTA activation), centered on VTA.

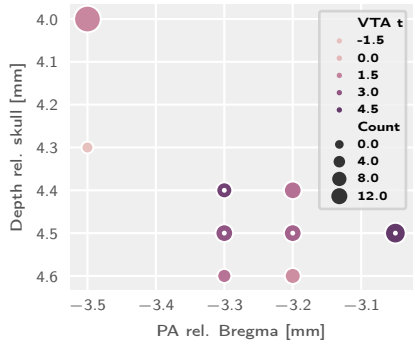

(c) VTA activation-based implant coordinate classification (dotted markers indicate best category).

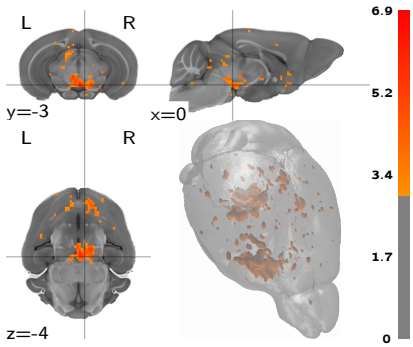

(d) Block stimulation of rostralmost implant category group, centered on VTA.

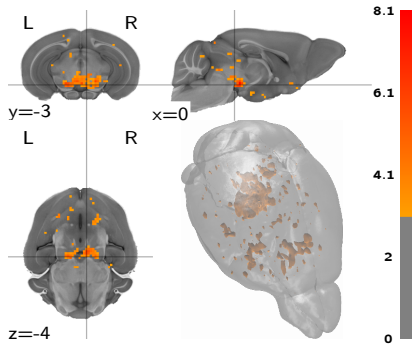

(e) Block stimulation of caudalmost implant category group, centered on largest cluster.

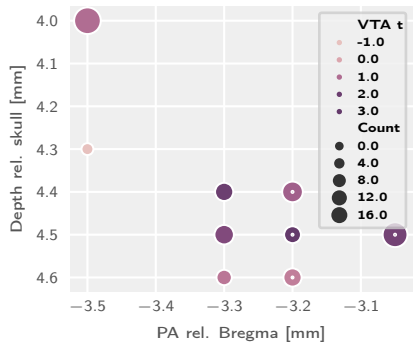

(f) PA-coordinate implant classification (dotted markers indicate rostralmost category).

Figure S2: PA-coordinate-based classification does not show a better projection segmentation than block trial-based classification. Depicted are t-statistic maps (centerd on largest cluster, thresholded at $t \geq 3$) of the second-level analysis for block stimulation protocols, divided into best and rejected **(a, b)**, or rostralmost and caudalmost **(d, e)**. All maps are adjusted for the wild type control stimulation effects.

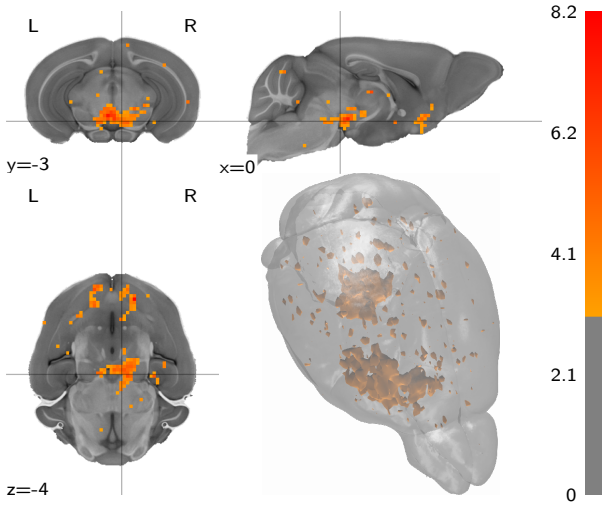

(a) Block stimulation, slices centered on largest cluster.

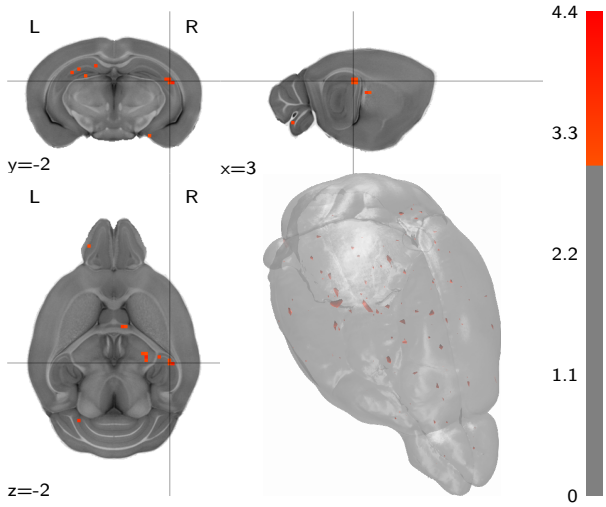

(b) Phasic stimulation, slices centered on largest cluster.

Figure S3: No negative activation patterns are salient upon block VTA stimulation, and no coherent activation patterns of any sort after phasic VTA stimulation. Depicted are t-statistic maps (thresholded at $|t| \geq 3$) of second-level analyses, divided by stimulation category and binning all implant coordinates. Slices are centered on the VTA coordinates (RAS $= 0.5/-3.2/-4.5$) and the largest cluster, respectively. All maps are adjusted for the wild type control stimulation effects.

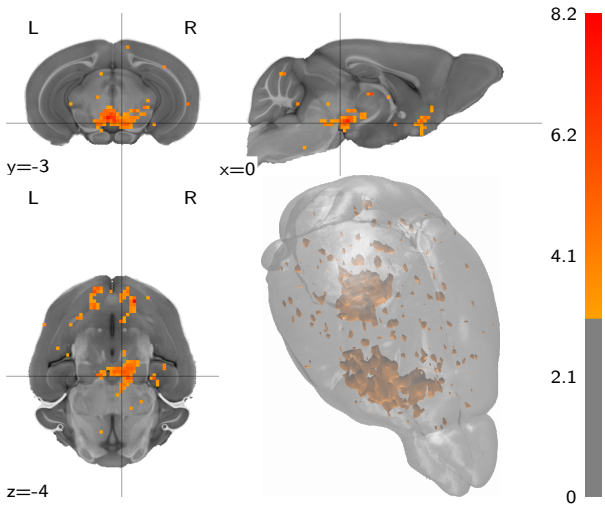

(a) Block stimulation of best implant category group

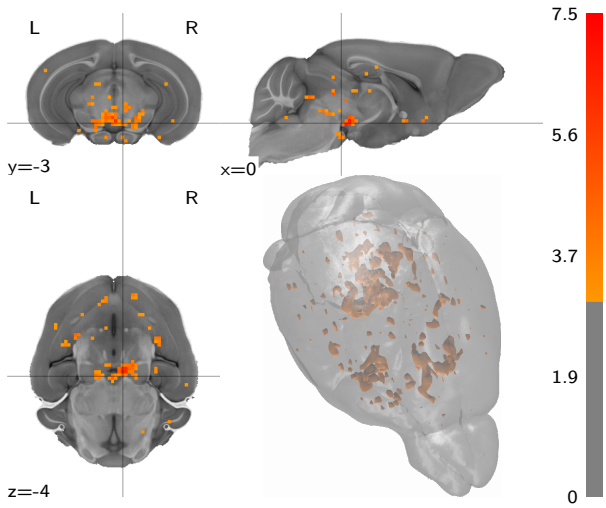

(b) Block stimulation of rejected implant category group.

Figure S4: The uncorrected population-level response to block stimulation does not significantly differ from the wild type control corrected results in figs. 3a and 3c. Depicted are t-statistic maps (thresholded at $t \geq 3$) of the second-level analysis for block stimulation protocols, divided by implant category group. Slices are centered on the VTA region of interest.

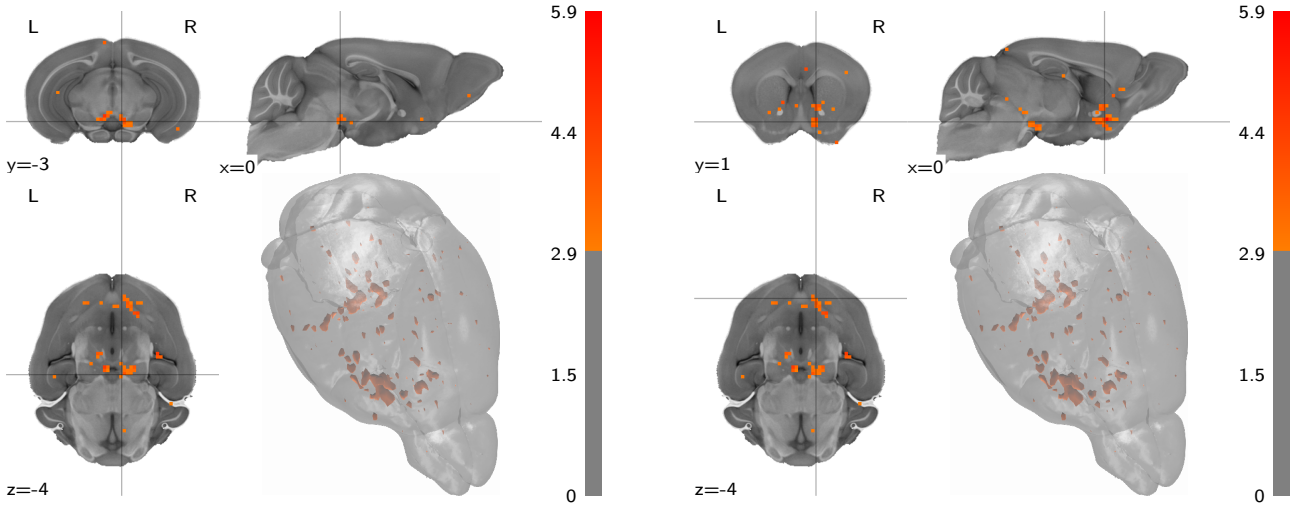

(a) Slices centered on VTA. **(b)** Slices centered on largest cluster.

Figure S5: Depicted are t-statistic maps (thresholded at $t \geq 3$) of the second-level analysis for block stimulation task VTA seed functional connectivity, observed in the best implant category, corrected for the negative control baseline. Slices are centered on the VTA coordinates (RAS $= 0.5/-3.2/-4.5$) and the largest cluster, respectively. This comparison is only provided for the sake of completeness and analogy with the stimulus-evoked analysis. Conceptually this comparison is not of primary interest, since seed-based functional connectivity attempts to include precisely the baseline functioning of the system into the evaluation.

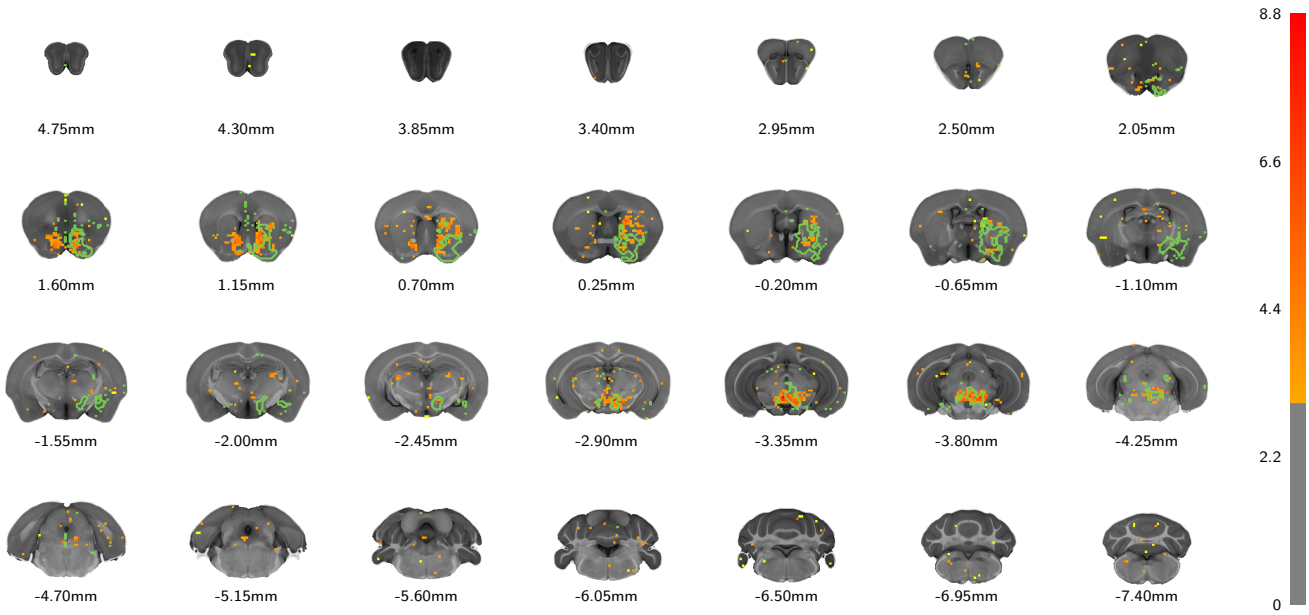

Figure S6: Coronal slice overlay, showing the VTA functional activation t-statistic heatmap (as in **fig. 3a**), and the VTA structural projection outline, both thresholded at $t \geq 3$. Interpretation of this figure as showcasing a complementarity in the patterns is cautioned, as qualitative inspection of thresholded data does not accurately capture variation in the statistic distributions. For statements regarding the compariosn of functional activation and structural projection, figs. 4a to 4c are more suitable.

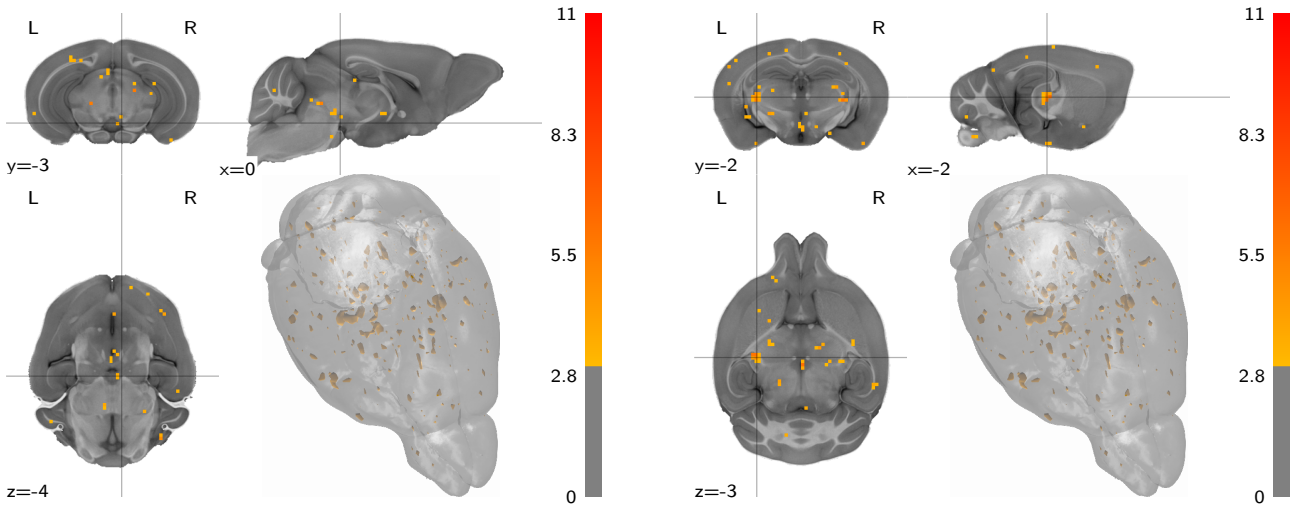

(a) Slices centered on VTA.

(b) Slices centered on largest cluster.

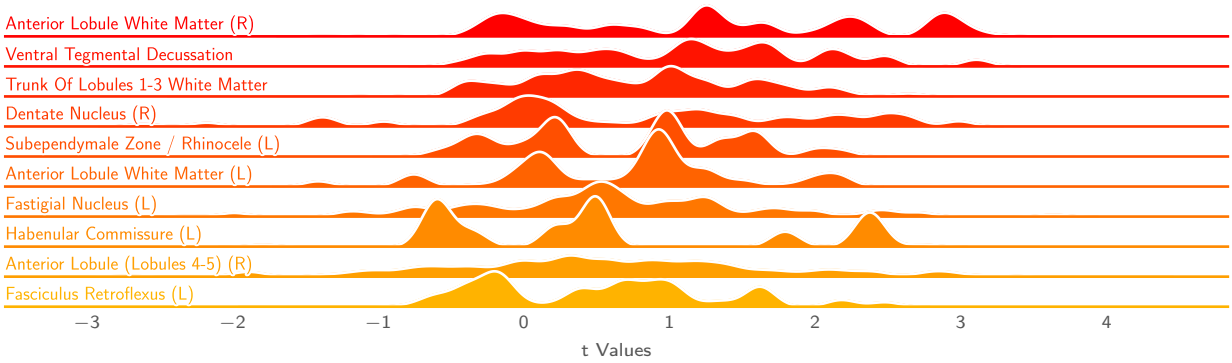

(c) Distribution densities of t-statistic values in the 10 most strongly activated areas.

Figure S7: Block stimulation in wild type control animals produces no large activation clusters, yet scattered activation hints at some visual excitation and heating artefacts. Depicted are volumetric population t-statistic maps **(a, b)** — thresholded at $t \geq 3$, as well as a break-down of activation along atlas parcellation regions **(c)**.